HAL
open science

11 B-MAS NMR approach to the boron adsorption mechanism on a glucose-functionalised mesoporous silica matrix

Cristina Sanfeliu, Ramón Martínez-Máñez, Félix Sancenón, Juan Pablo Soto, Pedro Amorós, Thierry Azaïs, M. Dolores Marcos

To cite this version:

Cristina Sanfeliu, Ramón Martínez-Máñez, Félix Sancenón, Juan Pablo Soto, Pedro Amorós, et al.. 11 B-MAS NMR approach to the boron adsorption mechanism on a glucose-functionalised mesoporous silica matrix. Microporous and Mesoporous Materials, 2018, 266, pp.232-241. 10.1016/j.micromeso.2018.02.016 . hal-01744281

HAL Id: hal-01744281

https://hal.sorbonne-universite.fr/hal-01744281v1

Submitted on 27 Mar 2018

HAL is a multi-disciplinary open access archive for the deposit and dissemination of scientific research documents, whether they are published or not. The documents may come from teaching and research institutions in France or abroad, or from public or private research centers.

L'archive ouverte pluridisciplinaire **HAL**, est destinée au dépôt et à la diffusion de documents scientifiques de niveau recherche, publiés ou non, émanant des établissements d'enseignement et de recherche français ou étrangers, des laboratoires publics ou privés.

^{11}B-MAS NMR Approach to the Boron Adsorption Mechanism on a Glucose-functionalisedfunctionalised Mesoporous Silica Matrix

Cristina Sanfeliu,[a,b,c] Ramón Martínez-Máñez,[a,b,c] Félix Sancenón,[a,b,c] Juan Soto,[a,b,c] Pedro Amorós,[d] Thierry Azaïs,[e] and Mª Dolores Marcos[a,b,c]*

[a] Instituto Interuniversitario de Investigación de Reconocimiento Molecular y Desarrollo Tecnológico (IDM), Universitat Politècnica de València, Universitat de València. E-mail: mmarcos@qim.upv.es

[b] Departamento de Química, Universitat Politècnica de València, Camino de Vera s/n, 46022, Valencia, Spain.

[c] CIBER de Bioingeniería, Biomateriales y Nanomedicina (CIBER-BBN).

[d] Institut de Ciència del Materials (ICMUV), Universitat de València, P.O. Box 22085, E-46071, Valencia, Spain.

[e] Sorbonne Universités, UPMC Univ Paris 06, CNRS, Collège de France, Laboratoire de Chimie de la Matière Condensée de Paris (LCMCP), 11 place Marcelin Berthelot, F-75005, Paris, France.

ABSTRACT: Boron chemistry has raised much interest because, despite the difference between necessities and toxicity being very narrow, it is still widely used in industrial processes. In a previous work we reported an adsorbent for boron extraction from water by the functionalisation of a UVM-7 mesoporous silica matrix with gluconamide moieties. The ability of this material to adsorb boron is based on its well-known affinity for coordinating the cis-diols present in attached saccharide. Although much research on the formation of boron esters with sugars and sugar derivatives in solution has been done, very few reports have dealt with the adsorption mechanism of boron onto functionalised materials in the solid state. Hence an in-depth study of the adsorption process was conducted in this paper. For this purpose, several solids with increasing boron contents were prepared from the gluconamide-functionalised UVM-7 material and an isothermal boron adsorption curve was obtained. The ^{11}B and ^{13}C MAS NMR techniques were used to characterise the obtained solids, and the simulation of the boron NMR and isothermal adsorption combined data was accomplished to enlighten the boron adsorption process. A model with three different coordination environments, two possible adsorption sites and the presence of oligomeric boron species allowed us to reproduce not only the isothermal boron adsorption curve, but also the evolution of the integrated areas for the signals in the ^{11}B MAS NMR spectra obtained for the different boron-containing gluconamide-functionalised UVM-7 materials.

Keywords: gluconamide-functionalised porous materials, boron adsorption modelling, ^{11}B MAS NMR.

1. INTRODUCTION

Boron has been extensively used in many industries, such as glass, ceramics, porcelain, cosmetics, semiconductors, carpets and fireproofing fabrics. Nowadays, the boron concentration in ground water increases day by day for both natural and anthropogenic reasons. Due to the use of boron-containing products, boron waste has become a serious problem. Eventually, it may pollute drinking water sources and lead to a series of environmental and health problems [1, 2]. Treatment methods to remove boron include coagulation-electrocoagulation, adsorption on oxides and membrane exchange resins [3-5]. Among them, the most effective method to remove boron from aqueous solutions is the adsorption technique because process requirements are simple and can be used in aqueous media with low boron concentrations.

Hybrid functional mesoporous materials have been recently applied in adsorption protocols, including the removal of boron from aqueous solutions by introducing polyol functional groups on the inner walls of mesoporous supports by the post-grafting method [6-9]. This design is based on the ability of boric acid to form chelate complexes with organic molecules that bear vicinal hydroxyl groups through esterification reactions [10]. Hence partial esterification may create 1:1 boron:polyol complexes in which a five- or six-member ring is formed. Complete esterification leads to the formation of bicyclic 1:2 boron:polyol complexes, as shown in Scheme 1.

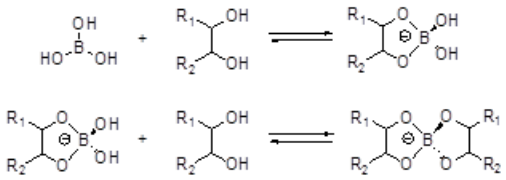

Scheme 1. Formation of mono- and bis-chelate borate esters with polyhydroxy compounds.

Boron mono-chelate complexes are quite labile and rapidly hydrolyse to their original components in aqueous solution, while bis-chelate complexes are thermodynamically more stable and almost indissociable in water. While boron complexation by adjacent hydroxyl groups in the polyol is commonly assumed, it has been evidenced that complexation across alternate hydroxyl groups is also possible, as demonstrated by ^{1}H NMR spectroscopy, ^{11}B NMR spectroscopy, circular dichroism and polarimetry [11-14].

Although much research has been done on borate esters of sugars and sugar derivatives in solution [15-18], very few reports have dealt with the adsorption mechanism of boric acid or borate onto functionalised materials in the solid state. Yoshimura and co-workers [19] studied the interaction between *N*-methylglucamine resin and borate. The combination of distribution and ^{11}B MAS NMR measurements revealed the formation of a 1:1 tetradentate complex of $B(OH)_4^-$ with the *N*-methylglucamine group. Nevertheless, this study only showed the pH dependence of borate esters formation in the solid state and no ^{11}B MAS NMR measurements in their resin-boric acid/borate system are presented. Thus, to the authors' knowledge, an in-depth

study on the mechanism involved in the adsorption of boron species by solid adsorbents, such as functionalised materials, has not yet been reported.

We have previously described the preparation of various materials and supports for boron removal from aqueous solutions [20-22]. These materials were built by grafting saccharide functionalities onto mesoporous silica scaffolds with different porous structures. However, no emphasis was made then in the adsorption mechanism terms, and only boron adsorption by the formation of chelate complexes with silica-attached hydroxyl groups was stated. Given the fact that the elucidation of the interactions between boron species and the anchored groups in the adsorbent materials should provide important information to develop new boron-selective efficient adsorbents, in this work we accomplished the synthesis and characterisation of boron-adsorbent materials with different boron contents. This time we used the very well-known UVM-7 mesoporous silica [23], functionalised with gluconamide moieties. In addition to typical characterisation techniques, the combination of boron-isothermal adsorption experiments with the ^{11}B MAS NMR spectroscopic analysis [24-27] of each obtained solid resulted in a powerful tool to elucidate the boron species present in the solid phase as a function of the boron concentration in aqueous media. Hence we herein present the synthesis and characterisation of boron adsorbents and the corresponding analysis of the boron complexation process onto active material. The obtained data offer relevant information about the interaction between boron species and the functional groups in the adsorbent.

2. EXPERIMENTAL SECTION

Chemicals: All the chemicals for the synthesis of mesoporous materials, tetraethyl orthosilicate (TEOS), sodium silicate, *n*-cetyltrimethylammonium bromide (CTAB), and triethanolamine

($TEAH_3$), were provided by Aldrich. For material functionalisation, (3-aminopropyl)triethoxysilane (**1**) and gluconolactone (**2**) were purchased from Aldrich. To prepare boron solutions, boron standard solution of 1,000 ppm was provided by Scharlab. To determine the boron concentration, azomethine-H was purchased from VWR.

Materials characterisation: Powder X-ray diffraction (PXRD) data were recorded on a Bruker D8 Advance diffractometer using Cu Kα radiation. PXRD patterns were collected in steps of 0.02°2θ within the angular range 0.65-10°2θ and in an acquisition time of 25 s/step. High and low-magnification SEM images were recorded by a Jeol JSM 6300 microscope. Samples were previously coated with Au-Pd. A TEM study was carried out with a Philips CM10 instrument which operated at 100 KV and was equipped with a CCD camera. Samples were gently ground in dodecane, and microparticles were deposited on a holey carbon film supported on a Cu grid. Nitrogen adsorption-desorption isotherms (-196°C) were recorded by a Micromeritics ASAP-2010 automated instrument. Calcined samples were degassed at 120°C and 10^{-6} Torr for 5 h prior to measurements. Surface areas were estimated by the BET model, and pore size dimensions and pore volumes were calculated by using the BJH method from the adsorption branch of the isotherms. Thermogravimetric analyses were performed on a TGA/SDTA 851e Mettler Toledo balance, with a heating programme that consisted of a heating ramp of 10°C per minute from 393 to 1,273 K and an isothermal heating step at this temperature for 30 min. The elemental analysis was run in a CE Instrument EA-1110 CHN Elemental Analyser. Spectrophotometric measurements were taken with a Lambda 35 UV/Vis Spectrometer (Perkin-Elmer Instruments).

NMR measurements: NMR spectra were recorded on a 16.3 T Advance 700 Bruker spectrometer with magic angle spinning (MAS). Samples were packed in 3.2 mm zirconia rotors and spun at 22 kHz. Larmor frequencies were $\nu_L(^1H)$ = 700.13 MHz, $\nu_L(^{11}B)$ = 224.6 MHz,

$\nu_L(^{13}C)$ = 176.07 MHz. ^{11}B spectra were recorded by a composite pulse sequence ($\pi/2$-π-π) ($\pi/2$ pulse = 1.5 μs) to suppress the background probe signal [28]. As the boron content varied in each sample, the number of co-added transients was adjusted to reach a reasonable signal-to-noise ratio: 147456, 73728, 64016, 41472, 36864 and 14576 for S1-B1, S1-B2, S1-B3, S1-B4, S1-B5 and S1-B6, respectively. Since the observed ^{11}B resonances displayed a symmetrical Gaussian line shape and did not exhibit any quadrupolar lineshape (see below), we safely assumed that the composite pulse sequence used for boron background suppression did not induce any spectral distortion in terms of line shape and relative intensities, and thus allowed a quantitative analysis of spectra. ^{13}C spectra were recorded by ^{1}H-to-^{13}C cross polarisation (CP) experiments with a contact time of 1.5 ms. ^{13}C CP MAS spectra were proton-decoupled during acquisition (SPINAL-64) with a ^{1}H radio-frequency field of $\nu(^{1}H)$ = 50 kHz. Recycle delays were 1.5 and 5 s for the ^{11}B MAS and ^{13}C CP MAS experiments, respectively. Spectra were referenced (δ = 0 ppm) to TMS for the ^{13}C and boric acid aqueous solution (0.1 M) for ^{11}B for comparisons with the data from reference 25.

Molecular modelling: Eleven structural varieties of the possible boroester complexes were studied computationally by the PM3 calculations applying the basis set included in the HYPERCHEM program package. Full geometry optimisations were performed on the isolated ions. Calculations were considered to have ended when the gradient norm reached 0.1. The boroester complexes geometries were calculated in an aqueous environment. After geometry optimisation, the values (reflecting the stabilities of the complexes) were compared and related to the experimental findings.

Synthesis of UVM7: The nanosized mesoporous UVM-7 silica was synthesised through a one-pot surfactant-assisted procedure in a homogeneous hydro-alcoholic reaction medium (water/triethanolamine). The general procedure, a modification of the so-called atrane route [23], is described in detail elsewhere. It is based on the use of a simple structural directing agent (such as *n*-cetyltrimethylammonium bromide, CTAB) and a complexing polyalcohol (triethanolamine), which results in silatrane complexes (relatively inert complexes that include triethanolamine-related ligand species) as hydrolytic precursors. To open the intrananoparticle mesopores, the surfactant was extracted from the as-synthesised mesostructured solid by chemical exchange using an HCl/ethanol solution (CTAB/H^+ exchange). Thus 1 g of mesostructured UVM-7 powder was suspended in a solution that contained 16 mL of HCl (37%) and 130 mL of ethanol (99%), and this mixture was heated at reflux (60°C) for 2 h under stirring. After renewing the HCl/ethanol solution and completing the extraction process, the suspension was stirred and heated again at 60°C for 16 h. The resulting mesoporous powder (UVM-7) was collected by filtration, washed with ethanol, and air-dried at 100°C.

Synthesis of S1: UVM-7 (1 g) was suspended in acetonitrile (40 mL) and heated at 120ºC in a Dean-Stark apparatus to remove the adsorbed water by azeotropic distillation in an inert atmosphere (Ar gas). Then to this suspension, (3-aminopropyl)triethoxysilane (10.7 mmol, step 1 in scheme 2) was added at room temperature. After 16 h, the solid (**SNH_2**) was filtered, washed (acetonitrile and water) and dried. As a last step, solid **SNH_2** (0.75 g) was suspended in methanol (50 mL), gluconolactone (10 mmol, step 2 in scheme 2) was added, and the mixture was stirred at room temperature for 48 h. The final solid **S1** was filtered, washed with water and dried (see scheme 1).

Synthesis of boron-charged materials: The mesoporous solids that contained different amounts of boron were prepared from **S1**. Boron adsorption was carried out by suspending **S1** (100 mg) in boron solutions at selected concentrations (50 mL). Suspensions were stirred for 16 h and then filtered. Final solids, with different boron contents (**S1-B1**, **S1-B2**, **S1-B3**, **S1-B4**, **S1-B5** and **S1-B6**), were washed (water), dried and stored for further NMR measurements. The boron concentration in the remaining solution was determined by the azomethine-H method. The difference between this value and the initial concentration gave the adsorbed amount in the final materials.

3. RESULTS AND DISCUSSION

Design and synthesis of the adsorbent material. The synthesis of the boron adsorbent material **S1** is shown in Scheme 2. Inorganic support UVM-7 mesoporous silica was selected for its high loading capacity and its easy chemical functionalisation. UVM-7 material is a mesoporous silica phase with a bimodal pore system prepared with tetraethylorthosilicate (as a silica source) and hexadecyltrimethylammonium bromide (as a templating agent). Hence the UVM-7 matrix can be described as bimodal porous silica constructed by the aggregation of pseudo-spherical mesoporous primary nanoparticles, with an average diameter of ca. 15-20 nm. These particles present a small intra-particle mesopore system that results from the template effect of the surfactant aggregates (acting as porogens as a result of their ulterior elimination). These small mesopores have a narrow size distribution and are organised in a disordered hexagonal array. These particles also present a second large inter-particle mesopore system that is generated while the nucleation and growth of primary mesoporous nanoparticles proceed. In practice, the formation of a continuous network from the soldered nanoparticles generates a disordered system of large void-pores (ranging from large-meso to macropores) that accounts for the observed

textural porosity [29-31]. The non-ordered nature of this large pore system is consistent with a formation mechanism that implies the collision and aggregation of primary nanoparticles. Thus on a micrometric scale, UVM-7 silicas present rough surfaces that result from the aggregation of pseudo-spherical clusters of mesoporous nanoparticles that define the large true textural macropores among them.

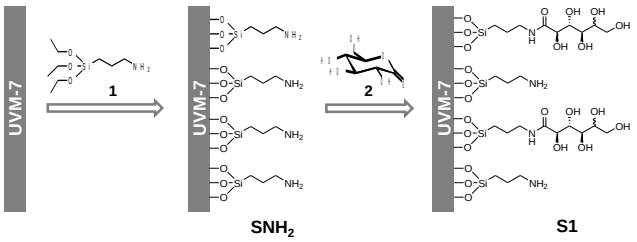

Scheme 2. Schematic representation of the synthesis of materials **SNH_2** and **S1**.

Knowing the affinity of boron aqueous species for cis-diol moieties, glucose molecules were selected as functional groups. As seen in Scheme 2, the UVM-7 support was functionalised in a first step with aminopropyl moieties through the reaction of the silanol moieties located on the surface with (3-aminopropyl)triethoxysilane (step 1 in scheme 2). This functionalisation step yields the **SNH_2** material. In a second step, the amino groups of **SNH_2** were reacted with gluconolactone (step 2 in scheme 2) to yield final solid **S1**.

The reaction between the grafted amino groups in **SNH_2** and gluconolactone to produce the final material **S1** gave a 53% yield (mol of glucose per gram of SiO_2 in **S1** related to the number of mol of amine per gram of SiO_2 in **SNH2**; see below). The moderate yield of the

amidation reaction was a clear consequence of the fact that the formation of bulky gluconolactone moieties would induce major pore blocking and steric hindrance. Despite the fact that the amine moieties in **SNH_2** are located mainly on the surface of wide textural pores, the reaction of the more accessible NH_2 groups with gluconolactone should induce some pore blocking and, consequently, the progress of the reaction was somehow disabled and led to a moderate yield. The final **S1** solid was then a bimodal pore material with gluconamide moieties grafted on its surface that contained cis-diol groups capable of reacting with boron species to yield boroester entities.

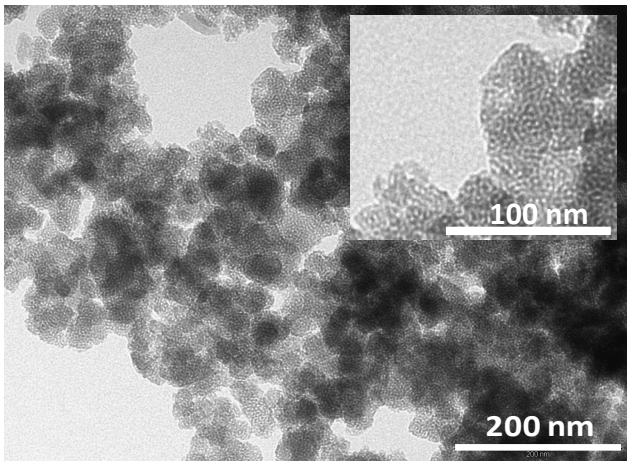

Figure 1. Representative TEM micrograph of the bimodal porous UVM-7 materials.

Characterisation of sorbents. Figure 1 depicts a representative image of the typical structure of the UVM-7 inorganic matrix. In this figure we can clearly see how the small mesoporous particles fuse together to give rise to the secondary interparticle pore system. The pseudo-hexagonal-ordered intraparticle mesopore system can also be observed inside the small particles.

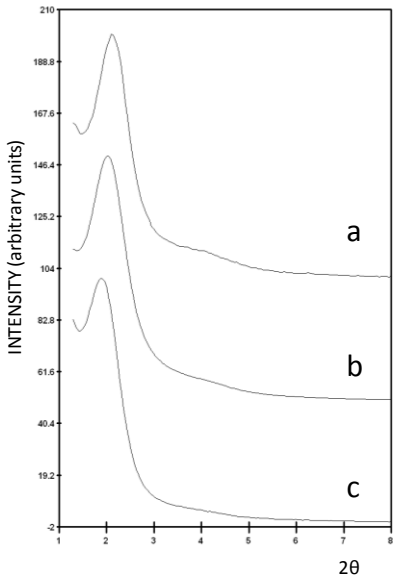

Figure 2. X-ray powder diffraction patterns of (a) as-synthesised (mesostructured) UVM-7, (b) chemically extracted UVM-7 silica and (c) functionalised solid **S1**.

Figure 2 illustrates the PXRD patterns that correspond to a representative sample of the UVM-7 material (a) before (mesostructured), (b) after (porous) template removal and (c) after the grafting protocol (solid **S1**). These PXRD patterns are characteristic of this kind of nanoparticulated mesoporous/mesostructured solids, prepared through surfactant-assisted procedures, which display at least one strong broad diffraction peak in the low angle region. In the three cases, the PXRD patterns indicate the relative order of the intra-nanoparticle mesopore (small pores) system and are clear proof of the presence of a certain pseudo-hexagonal order (broad small shoulder at around $4^{o}2\theta$). Hence we may infer that the organisation of the intraparticle mesopores in solid **S1** (curve c in Figure 2) is also preserved after the two-step functionalisation process.

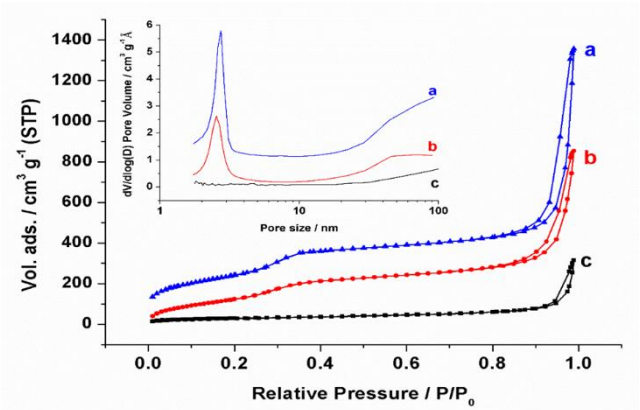

Figure 3. N_2 adsorption-desorption isotherms of (a) UVM-7 extracted material, (b) SNH2 sample and (c) S1. The inset shows the BJH pore size distributions from the adsorption branch of the isotherms. Curves have been y-shifted for clarity.

The N_2 adsorption-desorption isotherms quantitatively confirm the bimodal character of the UVM-7 material (Figure 3). As noted, the curve shows two well defined adsorption steps. The first one, at an intermediate relative pressure ($0.3 < P/P_0 < 0.5$), is characteristic of type IV isotherms and can be related to the capillary condensation of N_2 inside mesopores. The second step, at a high relative pressure ($P/P_0 > 0.8$), corresponds to the filling of large pores among primary nanoparticles. Hence the BJH pore size distribution shows the existence of both differentiated pore systems: first an intense narrow signal with a maximum at 2.7 nm ascribed to the surfactant generated pores; second a very wide pore distribution that expands up to large macropores (> 50 nm).

The specific surface areas, volumes and pore sizes were calculated from a Brunauer–Emmet-Teller (BET; specific surface area) treatment of the isotherm [32], and the Barret–Joyner–Haselda (BJH; volumes and pore size) method [33], respectively, and are shown in Table

1. UVM-7 materials show a large surface area (878 m^2 g^{-1}) and an interparticle pore diameter bigger than 50 nm, which would allow a high degree of organic functionalisation. The N_2 adsorption-desorption isotherm of the solid modified with APTES (**SNH_2**) is qualitatively similar to that of the parent UVM-7 silica. However, the incorporation of the amine groups leads to a certain reduction in both the BET specific surface area and the BJH pore volume (Table 1). In any case, the **SNH_2** solid preserved the bimodal porosity of the UVM-7 silica and the typical enhanced accessibility to the active amine groups. The observed reduction in the BJH intraparticle mesopore size after functionalization with APTES must be associated with the anchoring of the propylamine moiety onto the whole surface, including the internal mesopores surface (whose size slightly reduces). Finally, sugar incorporation (solid **S1**) must induce significant blocking, especially of intraparticle mesopores, and a very marked reduction in both the BET area and the mesopore volume was detected. In fact the estimated BET area could be associated mostly with the large interparticle mesopore system (whose porosity is preserved). At this point, it is important to take into account the sample preparation conditions for measuring the N_2 adsorption in the ASAP2020 instrument (very low pressure and moderate temperature). Under these conditions, major dehydration phenomena must occur in the environment of the large sugar molecules to provoke the blocking of the intraparticle mesopores, by hindering their filling with N_2. However under the boron adsorption working conditions (water solution), the pores system should present quite a high permeability for boron species (see below).

Table 1. Selected physical data of **UVM-7**, **SNH2** and **S1** solids.

Material	BET specific surface area (m^2g^{-1})	Intraparticle pore[a] (nm)	Small pore volume[a] (cm^3 g^{-1})	Interparticle pore[a] (nm)	Large pore volume[a] (cm^3 g^{-1})
UVM-7	878±2	2.77(5)	0.72(6)	54.2(8)	1.30(5)
SNH_2	632±3	2.57(8)	0.57(7)	46.6(9)	0.87(7)
S1	108±4	~1.9-2.0[b]	0.10(7)	42.4(9)	0.45(8)

[a] Pore sizes and volumes determined by applying the BJH model on the adsorption branch of isotherms. A cut-off value of P/P_0= 0.75 was used to independently calculate the pore and size of the intraparticle mesopores (P/P_0 < 0.75) and the interparticle textural ones (P/P_0 > 0.75). [b] The low signal intensity in the pore size distribution hinders the method from achieving precise determinations.

For all the organic-inorganic hybrid materials, one key point associated with their characterisation is functionalisation degree determination. The contents in the organic groups (i.e. amine and gluconamide) in materials **SNH_2** and **S1** were determined by thermogravimetric and elemental analyses. From the elemental analyses of C, H, N, it is possible to determine the amount of the binding groups contained in the corresponding material (calculated in millimoles per gram of SiO_2, mmol g^{-1} SiO_2) using Equation (1):

$$\boldsymbol{\alpha_A} = \frac{\Delta \boldsymbol{W_i}\% \times \mathbf{1000}}{\Delta \boldsymbol{W_{SiO_2}}\% \times \boldsymbol{nM_i}} \text{ (mmol g}^{-1}\text{ SiO}_2\text{)} \qquad (1)$$

where $\Delta W_i\%$ (i = C, N) are the weight percentages of carbon or nitrogen, M_i is the corresponding atomic weight and n is the number of atoms per molecule of the corresponding element. $\Delta W_{SiO2}\%$ is the inorganic SiO_2 content as a weight percentage. These experiments allowed us to estimate the total amount of organic material in **SNH_2** and **S1**. In line with this, a degree of functionalisation of 2.45 mmol of amine per gram of SiO_2 was obtained for solid **SNH_2**, whereas 1.29 mmol of glucose per gram of SiO_2 was acquired for **S1**. Bearing in mind both contents, the amidation reaction yield can be calculated as being about 53%.

We also calculated the average coverage, β_{gluc}, as the number of gluconamide molecules per nm^2 using Equation (2) in which α_A is the anchored group content ($mmol \cdot g^{-1}$ SiO_2), S is the specific surface ($m^2 \cdot g^{-1}$) of the UVM-7 material (Table 1) and N_A is the Avogadro's number.

$$\boldsymbol{\beta_A = \alpha_A \times 10^{-3} \times S^{-1} \times 10^{-18} \times N_A = \alpha_A \times S^{-1} \times 602,3} \qquad (2)$$

thus solid **S1** presents 0.88 gluconamide molecules per nm^2, which corresponds to an average distance of 1.1 nm between the vicinal groups attached to the surface.

The characterisation of the organic matter in solids **SNH_2** and **S1** was examined through the ^{13}C NMR studies done with both materials. These studies allowed us to confirm the correct performance of both the functionalisation reaction of the UVM-7 mesoporous matrix with APTES (reactant **1** in scheme 2) and also the amidation reaction of solid **SNH_2** with gluconolactone (reactant **2** in scheme 2). The ^{13}C CP MAS NMR spectra of solids **SNH_2** and **S1** are shown in Figure 4. The ^{13}C NMR spectrum of solid **SNH_2** (curve b in Figure 4) displays three resonances within the 10-50 ppm interval, which are assigned to the propyl chain that links the amino moiety to the inorganic scaffold. In more detail, the signal that appears at ca. 10 ppm can be ascribed to the carbon atom of the methylene moiety neighbour to the Si atom in the inorganic support, whereas the signal at ca. 45 ppm is due to the carbon atom of the methylene moiety directly linked to the amino group. Upon changing to solid **S1**, the ^{13}C NMR spectrum displays the same signals within the 10-50 ppm interval ascribed to the propyl linker, whereas other signals appeared within the 62-75 ppm interval and at ca. 170 (see curve (a) in Figure 4). The new signals were ascribed to the gluconamide moiety in **S1**, formed through an amidation reaction between amine moieties and gluconolactone. The broad signals that appeared within the 62-75 ppm interval are ascribed to the C-OH carbons of the "saccharide" units, whereas the signal at ca. 170 ppm was due to the amide carbon produced during the amidation process.

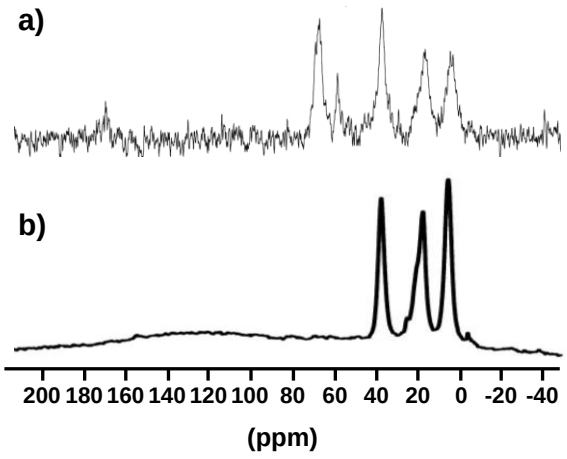

Figure 4. The ^{13}C CP MAS NMR spectrum of (a) **S1** and (b) **SNH$_2$**.

Boron-charged solids. Boron can be adsorbed on the functionalised materials if we consider that boric acid is able to link poly-ol groups to form a chelate complex [34]. Hence we expected boron to form both mono-chelate and bis-chelate complexes with the glucose groups attached to the adsorbent [24, 26]. In order to clarify the boron adsorption mechanism onto the solid and the stoichiometry of the formed complexes, several materials with different amounts of adsorbed boron were prepared and analysed by ^{11}B and ^{13}C MAS NMR.

All the boron-containing materials were prepared from **S1**. Hence different samples of solid **S1** (100 mg each time) were suspended in boron solutions at diverse concentrations (50 mL, from $1.92 \cdot 10^{-4}$ to $3.8 \cdot 10^{-2}$ mol dm^{-3}), filtered, and finally washed to remove free boric acid and physisorbed borates. This protocol yielded six different solids (**S1-B1**, **S1-B2**, **S1-B3**, **S1-B4**, **S1-B5** and **S1-B6**) with distinct boron concentrations. In each case the corresponding boron

content was determined following the azomethine method [35]. Table 2 shows the quantity of boron adsorbed in each prepared material, first as an absolute value (mmol of boron per gram of solid) and then as a value relative to the adsorbent gloconamide content (mmol of boron per mmol of gluconamide, considering a gluconamide content for **S1** of 0.86 mmol per gram of solid).

Table 2. Boron content in solids **S1-B1** to **S1-B6** (absolute and relative to the anchored glucose).

Material	B ads	
	mmol B/ g solid	mmol B/ mmol glucose
S1-B1	0.019	0.02
S1-B2	0.096	0.11
S1-B3	0.260	0.30
S1-B4	0.393	0.46
S1-B5	1.15	1.3
S1-B6	1.85	2.2

The high relative boron content obtained for solids **S1-B5** and **S1-B6** is indicative of a more than one boron coordination per anchored glucose group. In fact polyalcohols are able to form complexes of 2:1, 1:1 and 1:2 stoichiometries upon borate complexation. The formation of one or several complexes in our solid materials may be a function of the boron/gluconamide ratio. Accordingly in solid **S1-B1** (with a lower boron/gluconamide ratio) the formation of the bischelate 2:1 gluconamide-borate complex could be expected. With increasing borate concentrations, a monodentate 1:1 gluconamide-borate complex would be formed and it could coexist in the adsorbent with the firstly formed bis-chelate. At higher boron/gluconamide ratios

(as in solids **S1-B5** and **S1-B6**), more adsorption sites would be needed and monodentate 1:1 gluconamide-borate positions would be predominant.

^{13}C MAS NMR studies. The different solids prepared in this paper (**S1** and **S1-B1** to **S1-B6**) were studied by ^{13}C CP MAS NMR spectroscopy. The studies carried out in aqueous solutions indicated that upon borate ester formation, shifts of 3-10 ppm to a higher frequency were usually observed for the ^{13}C nuclei in the borate ester ring. To support the Discussion, Figure 5 shows the schematic structure of the grafted gluconamide with the carbon atoms' numbering assignment.

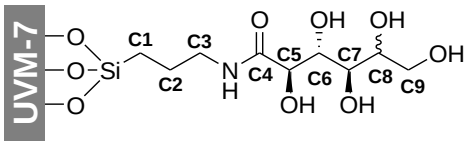

Figure 5. Structural formula of the gluconamide group with the numbering scheme used in the text.

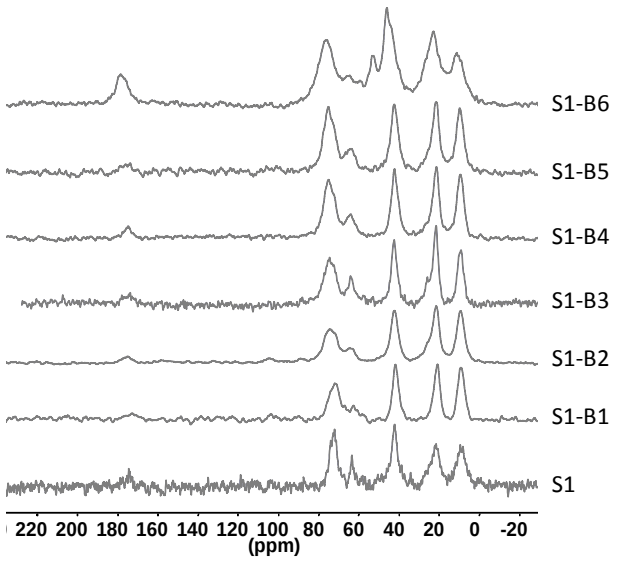

Figure 6. The ^{13}C CP MAS NMR spectra of solids **S1** to **S1-B6**.

Figure 6 displays the ^{13}C CP MAS NMR spectra and Table 3 is a full list of the corresponding chemical shifts of solids **S1**, **S1-B1**, **S1-B2**, **S1-B3**, **S1-B4**, **S1-B5** and **S1-B6**. The ^{13}C MAS NMR spectra of solid **S1** present six signals from the different environments surrounding the carbon atoms. The signals of the propyl linker carbon atoms (C1, C2 and C3 in Figure 6) appear at ca. 10, 21 and 42 ppm, respectively. When dealing with gluconamide signals, the methylene linked directly to a hydroxyl group (C9 in Figure 6) was related to the resonance centred at 63 ppm, whereas the broad signal centred at ca. 72 ppm was due to the overlapping of the resonances of carbon atoms in CH-OH groups (C5, C6, C7 and C8 in Figure 6). Finally, the signal of the carbon atom of the carbonyl group (C4 in Figure 6) was ascribed to the resonance at 174 ppm. Addition of small boron quantities (below the gluconamide content), as in solids **S1-B1**, **S1-B2**, **S1-B3** and **S1-B4**, induced negligible changes in the carbon signals of the propyl linker. However, the signals of the carbon atoms that bore hydroxyl moieties underwent moderate downfield shifts. In this respect, the signal of C9 shifted from 63 to 64.2 ppm upon changing from **S1** to **S1-B4**, whereas the signals of the C5-C8 carbons also shifted from 72 to 75.4 ppm. The carbonyl peak underwent a downfield shift from 174 to 175.2 ppm. These moderate downfield shifts (1.2 ppm for C9, 3.4 ppm for C5-C8 and 1.2 ppm for C4) of the carbon atoms of the gluconamide moiety were ascribed to the formation of bischelate $(\alpha,\beta)_2$-BL_2 and monochelate (α,β)-BL complexes. With higher boron contents (as in solids **S1-B5** and **S1-B6**), the signals of the carbons of the gluconamide moieties once again underwent moderate downfield shifts, but the most important feature of the ^{13}C NMR spectra were the changes observed for the propyl linker for solid **S1-B6**. Accordingly, the signals centred at 10 (C1) and 21 (C2) ppm shifted to 11.0 and 23.3 ppm, respectively. Moreover, the resonance of C3 was modified to a complex signal composed of a main resonance with a maximum at 46.5 ppm and

an additional resonance at 53.5 ppm. These downfield shifts were tentatively ascribed to the fact that a large amount of adsorbed boron would modify the chemical environment of the surroundings, even for the carbon atoms of the propyl linker, particularly C3.

Table 3. The ^{13}C CP MAS NMR chemical shifts of solids **S1** to **S1-B6**.

Material	δ C4 GLUC (ppm)	δ C5,6,7,8 GLUC (ppm)	δ C9 GLUC (ppm)	δ C3 APTES (ppm)	δ C2 APTES (ppm)	δ C1 APTES (ppm)
S1	174,0	72,6	63,5	42,6	21,6	9,6
S1-B1	174.0	72.6	63.4	42.3	21.4	9.6
S1-B2	175.2	74.6	64.8	42.9	21.7	9.6
S1-B3	175.2	74.9	64.5	42.8	22.0	9.5
S1-B4	175.2	75.4	64.2	42.5	21.6	9.6
S1-B5	176.6	75.3	64.0	42.5	21.6	9.8
S1-B6	178.8	76.8	65.8	46.5 and 53.5	23.3	11.0

^{11}B MAS NMR studies. Figure 7 displays the ^{11}B MAS NMR spectra of the six materials (**S1-B1** to **S1-B6**) prepared with increasing boron contents inside the **S1** adsorption matrix. The ^{11}B MAS NMR spectra displayed three different resonances at around -5.8, -12 and -17 ppm, which are characteristic of at least three distinct chemical environments in the 4-fold coordination where Boron was surrounded by 4 oxygens in a tetrahedral geometry. This rather high symmetric geometry led to weak quadrupolar coupling constants and the ^{11}B resonances did not exhibit any quadrupolar lineshape in the high static magnetic field used in this study (16.3 Tesla). ^{11}B resonances displayed a symmetrical Gaussian line shape, where the line width was probably dominated by a distribution of chemical shifts.

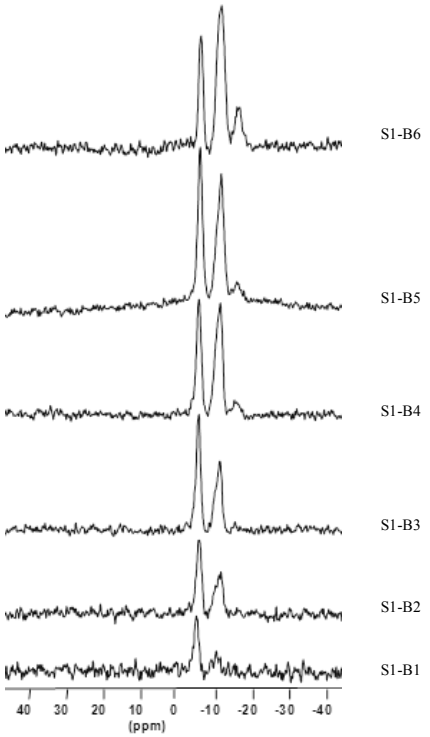

Figure 7. The ^{11}B MAS NMR spectra for solids **S1-B1** to **S1-B6** that contained different amounts of borate.

Several studies about the boron complexation with polyalcohols and saccharides in solution using ^{11}B NMR measurements have been conducted. These studies have paid attention to the identification of the ^{11}B resonance signals in the different complexes with the polyhydroxy compounds formed in solution. Van Duin and co-workers [25] studied the complexation of boron with a series of polyols and polyhydroxycarboxylates in aqueous solution. These authors observed signals at: -9.9 ppm, due to the formation of the $(\alpha,\beta)_2$-BL_2 bischelate complex; at -13.3 ppm, due to the formation of the (α,β)-BL monochelate complex; at -16.7 ppm, due to the

formation of the (α,γ)-BL monochelate complex; at -18.5 ppm, due to the formation of the $(\alpha,\gamma)_2$-BL_2 bischelate complex (see Scheme 3).

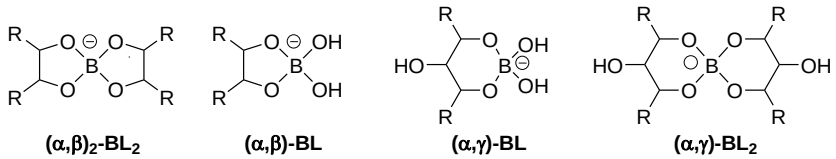

Scheme 3. Representative complexes formed between boric acid and polyol molecules.

Table 4. Relative integration of the signals appearing in the ^{11}B NMR spectra for the solids with increasing boron contents.

Material	% (-5.8 ppm)	% (-12 ppm)	% (-17 ppm)
S1-B1	67.1	32.9	0.0
S1-B2	55.3	44.7	0.0
S1-B3	53.7	44.7	1.6
S1-B4	38.7	55.2	6.1
S1-B5	41.6	51.2	7.2
S1-B6	24.8	59.5	15.6

As seen in Figure 7, solid **S1-B1**, with the lowest boron content, shows a symmetrical signal centred at -5.8 ppm (full width at half maximum FWHM ~ 1.6 ppm), which may be ascribed, following the above-mentioned studies in solution, to the $(\alpha,\beta)_2$-BL_2 bischelate complex. The formation of this bischelate complex at lower boron concentrations could be explained by bearing in mind the high availability of gluconamide moieties and the stability of the bis-bidentate borate complex. Addition of increasing quantities of boron (solids **S1-B2** and **S1-B3**) induced the clear emergence of a broader signal centred at -12 ppm (FWHM ~ 2.8 ppm), which was almost visible in the first spectra. Following Van Duin assignation, we could relate

this signal to the formation of the (α,β)-BL mono-chelate complex. Nevertheless given the Gaussian lineshape of this ^{11}B resonance, we believe that the line width of this peak was dominated by a distribution of ^{11}B chemical shifts, which could be induced by a local disorder due to the complexation to the flexible chains of the gluconamide group. Indeed flexibility would be greater for monochelate compared to the bischelate complexes as degrees of freedom lowered in the latter case to induce the difference in the line width observed experimentally between resonances -5.7 and -12 ppm. It Figure 7 we see that upon incrementing the amount of available boron to be adsorbed onto the polyol moieties, the relative area of the mono-chelate complex peak increased in relation to the area of the bis-chelate one. When integrating the corresponding signals, we can see that the **S1-B2** and **S1-B3** complexes coexist at a nearly 1:1 bis-chelate to mono-chelate ratio (see Table 4 for the relative integration of the signals in the ^{11}B NMR spectra for the prepared solids). If the available amount of boron was allowed to increase, a new broad peak with a chemical shift of -17 ppm (FWHM ~ 2.6 ppm) would also appear (see Figure 7). This new peak could be ascribed to the formation of the (α,γ)-BL monochelate complex. From Hyperchem [36] calculations it can be seen that the (α,γ)-dyol positions were also available when occupying the (α,β)-dyol positions (see Figure 8).

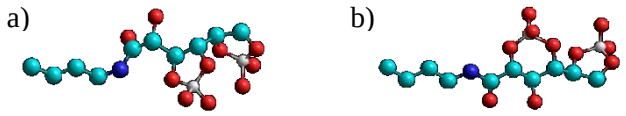

Figure 8. Hyperchem simulation of a) the (α,β)-BL mono-chelate complex and b) the (α,γ)-BL monochelate complex in the presence of an (α,β)-BL complex already formed at the end of the same gluconamide molecule.

Hence we could state that the first site for boron to be adsorbed was the highly stable bis-chelate coordinating place and the other mono-chelated sites started to be occupied only when these positions were highly engaged, with the (α,β)-diol preferred against the (α,γ)-diol ones. This fact clearly indicates that the (α,γ)-BL complex was the least stable and its formation was less favoured by the fact that the small boron atom size, compared with oxygen and carbon, better fitted the formation of the 5-membered ring chelate than the 6-membered one.

However, the study of Van Duin and co-workers was performed under experimental conditions for which the predominant species of boron was boric acid, $B(OH)_3$. It is well-known that with increasing boron concentrations, a number of polyborates could appear in solution [37] and more complicated species could be considered when boron was made to react with polyol molecules (see Scheme 3). In this way, Salentine [38] also used ^{11}B MAS NMR techniques to study the presence of polyborate species in solution. He reported the emergence of a broad signal centred at -18 ppm when the boron concentration rose to 0.15 M. Under our experimental conditions, the presence of polyborate species should be taken into account. Hence the upfield peak could also be contemplated to contain the resonance of chelates between the polyol molecules and the different polyborate species (see Scheme 4).

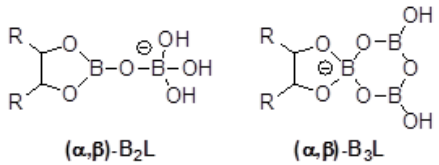

Scheme 4. Possible complexes formed between polyol molecules and polyborates species.

2D homonuclear ^{11}B correlation experiments would be an alternative to determine the presence of polyborate species, particularly for the samples that possess high boron content (S1-

B4, S1-B5, S1-B6). Nevertheless, these experiments suffer lower sensitivity compared to 1D MAS experiments. In our case, the total experimental acquisition time for the 1D MAS experiments to reach a reasonable signal-to-noise ratio was rather long (between 6 h and 61 h, depending on boron content). Hence recording 2D homonuclear 11B correlation experiments would be time-consuming.

By way of conclusion, the ^{11}B and ^{13}C MAS NMR studies indicated that at least three main complexes were formed upon the boron and the grafted gluconamide moieties in **S1** interaction. Whereas the ^{13}C MAS NMR measurements have shown a degree of interaction between boron species and the attached carbon chains, the ^{11}B MAS NMR spectra have provided information about the chemical nature of the formed complexes (bischelate or monochelate involving α,β or α,γ-diols).

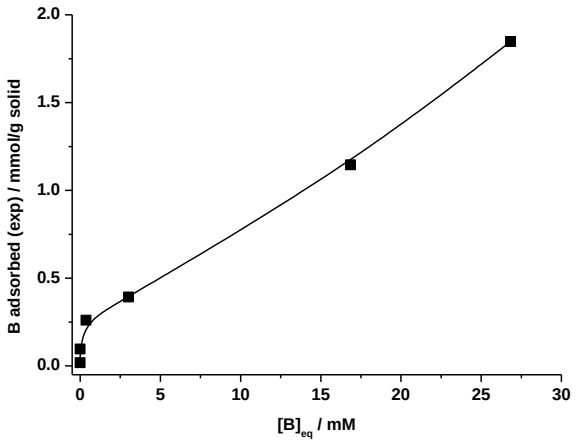

Figure 9. Boron adsorption isotherm: squares correspond with the experimental boron content of solids **S1-B1** to **S1-B6** and the solid line to the calculated boron content from the Langmuir-Freundlich model essayed for boron adsorption.

Boron adsorption isotherm. In order to gain further insight into the boron adsorption process, the corresponding isothermal adsorption experiments were performed. In Figure 9 the amount of adsorbed boron per gram of adsorbent is represented as a function of the equilibrium boron concentration in solution. The first part of the curve shows a typical profile of a Langmuir adsorption process. However, the last part of the curve, which accounts for the formation of solids **S1-B5** and **S1-B6,** shows an increasing profile that could correspond to a multilayer adsorption process. In Figure 9 the solid line shows the values obtained with a model that includes the occupation of a non-specific Langmuir position and a multilayer Freundlich adsorption mechanism. These values were obtained using the Solver tool implemented in the Microsoft Excel programme [39] and the used formula was:

$$n(B_{ads})_{total} = \frac{n(B_{ads})_1 * K_1 * [B_{eq}]}{1 + K_1 * [B_{eq}]} + K_\beta * [B_{eq}]^{\frac{1}{\beta}} \quad (3)$$

where $n(B_{ads})_{total}$ is the total number of mols of boron adsorbed per gram of adsorbent; $n(B_{ads})_1$ is the number of mols of boron adsorbed following Langmuir-type behaviour; K_1 is the corresponding adsorption constant; K_β is the Freundlich constant; β is the corresponding Freunlich exponent; $[B_{eq}]$ is the boron concentration of the solution in equilibrium with the corresponding solid. The adjustment was made by minimising the total standard deviation:

$$SD = \sqrt{\frac{\sum_1^6 \left[n(B_{ads})_{exp} - n(B_{ads})_{calc} \right]_i^2}{5}}$$

The combination of Langmuir and Freundlich models has been previously applied to fit the adsorption of boron from an aqueous solution using chelate adsorbents [40]. In our case the adjustment of the calculated data to the experimental values was quite good, as seen from the adjustment in Figure 9 and the data in Table 5. However, the obtained information is not very useful because the adsorption process must be more complex than that expressed by only a Langmuir constant and a general multilayer adsorption process. Our aim was to gain further insight into the boron adsorption process and to differentiate among the several possible coordination positions that the anchored glucose molecules may offer boron atoms. Hence we thought about combining the experimental adsorption data and the integrated areas obtained from the ^{11}B MAS NMR spectra.

Table 5. Results obtained from the Langmuir and Freundlich model essayed for boron adsorption.

Langmuir adsorption site	n (mmol/g solid)	0.27
	K	151
Freundlich multilayer	K_β	0.026
	β	1,24
Minimised parameter	Global Standard Deviation	0.011

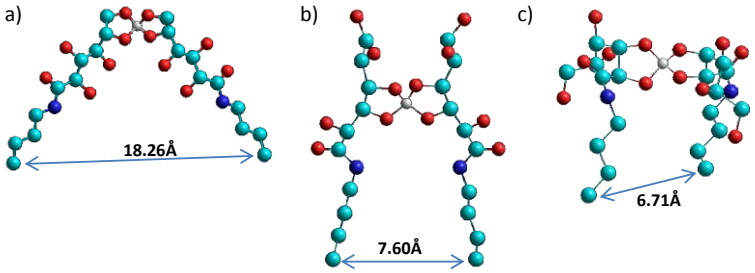

Figure 10. Hyperchem minimised bis-chelate boron complexes at different positions: a) (α,β-BL_2^-) (5,6); b) (α,β-BL_2^-) (3,4); c) (α,β-BL_2^-) (2,3).

As mentioned above, we assumed the existence of two different and possibly simultaneous adsorption positions: one at the end of the glucose molecules (*site E*) and the other that involved the other hydroxyl groups, which provide a more internal position (*site I*). From all the possible combinations made to coordinate boron with the anchored glucose molecules, we firstly assumed that bis-chelate complexes would form at external positions (*site E*) as they would show easier simultaneous coordination of two neighbouring molecules with the same boron atom. Hyperchem minimisation calculations (see Figure 10), also supported this idea as we found that the bis-chelate formed at the external position would need a maximum distance between gluconamide moieties of 18.23 Å. The average distance between gluconamide moieties in S1 was calculated as 10.7 Å, which is too long for the maximum distance needed for the formation of the bis-chelate complex at the internal position.

We then considered that this external position could be competitively occupied by the (α,β)-BL mono-chelate complexes, and hence we considered a competition equilibrium. For *site E*, the formation of mono-chelated complexes was contemplated and the equilibrium for the formation of both the (α,β)-BL and (α,γ)-BL complexes was taken into account. Hence the equilibrium reactions we used are:

Coordination equilibria at *site E*:

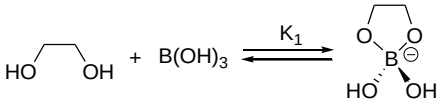

$$K_1 = \frac{\theta_{BLPE}}{(B(OH)_3)\theta_{LE}}$$

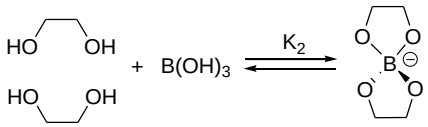

$$K_2 = \frac{\theta_{BL2}}{(B(OH)_3)\theta_{LE}}$$

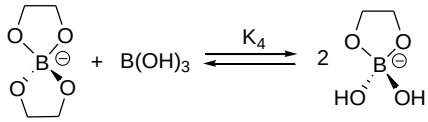

$$K_4 = \frac{\theta_{BLPE}}{(B(OH)_3)\theta_{BL2}}$$

Coordination equilibria at *site I*:

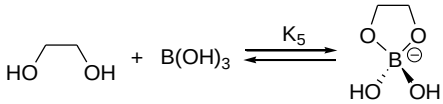

$$K_5 = \frac{\theta_{BLPI}}{(B(OH)_3)\theta_{LI}}$$

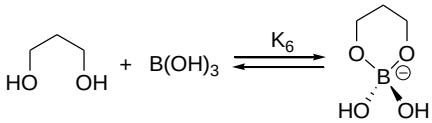

$$K_6 = \frac{\theta_{BLHI}}{(B(OH)_3)\theta_{LI}}$$

where θ values states for the fraction of adsorption sites:

$$\theta_i = \frac{n_i}{n_{total}}$$

and BL_2 refers to the (α,β)bis-chelate complex, *BLPE* and *BLPI* refer to the (α,β)mono-chelate complexes at *site E* and *site I* respectively, *BLHI* refers to the (α,γ)mono-chelate complex and *LE* and *LI* refer to the free positions at *site E* and *site I*, respectively. With this model, the evolution

of the isothermal adsorption curve was simulated after considering the adsorbed boron atoms at both positions:

$$n(B_{ads})_{total} = n(B_{ads})_{site\ E} + n(B_{ads})_{site\ I} \quad (4)$$

where:

$$n(B_{ads})_{site\ E} = n(B_{ads})_{BL_2} + n(B_{ads})_{BLPE} \quad (5)$$
$$n(B_{ads})_{site\ I} = n(B_{ads})_{BLPI} + n(B_{ads})_{BLHI} \quad (6)$$

The values of the number of boron mols adsorbed at each position were obtained by manually adjusting the above-defined equilibrium constants to achieve the best agreement with the experimental data:

$$(IA_{peak\ 1})_i * n(B_{ads})_{total\ i} = n(B_{ads})_{BL2\ i}$$
$$(IA_{peak\ 2})_i * n(B_{ads})_{total\ i} = n(B_{ads})_{BLPE\ i} + n(B_{ads})_{BLPI\ i}$$
$$(IA_{peak\ 3})_i * n(B_{ads})_{total\ i} = n(B_{ads})_{BLHI\ i}$$

where $(IA_{peak\ 1})$, $(IA_{peak\ 2})$ and $(IA_{peak\ 3})$ are the integrated areas of the absorption signals centred at -5.8 ppm (peak 1), -12 ppm (peak 2) and -17 ppm (peak 3) in the ^{11}B NMR spectra and $n(B_{ads})_{total}$ is the total adsorbed boron. Although this calculation could reproduce the first part of the curves, in order to simulate the final increase of the curves related with peak 2 and peak 3 the coordination of polyborate species to the adsorbent should be taken into account. Following the work published by Salentine [38], we considered that the adsorption which appeared at -12 ppm and -17 ppm not only contained the adsorption from the (α,β)-monochelate and (α,γ)-monochelate complexes, respectively, but also the resonance from the boron trimer and pentamer. Then new equilibria were considered:

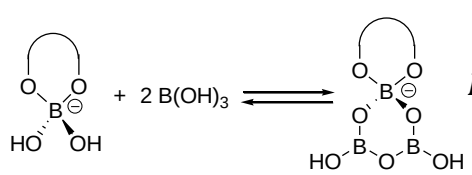

$$K_{O3} = \frac{\theta_{O3}}{(B(OH)_3)^2 \theta_{BL}}$$

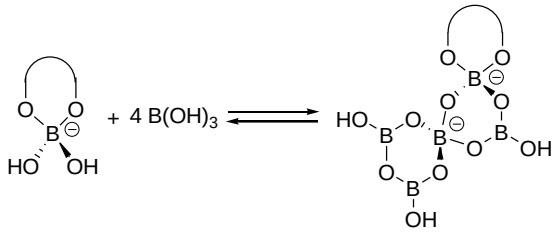

$$K_{O5} = \frac{\theta_{O5}}{(B(OH)_3)^4 \theta_{BL}}$$

where θ_{O3} and θ_{O5} state for the fraction of occupied sites by the trimers and pentamers species, and θ_{BL} the fraction of occupied sites with any monochelate complexes. Hence the considered adjustment is:

$$(IA_{peak\ 1})_i * n(B_{ads})_{total\ i} = n(B_{ads})_{BL2i}$$
$$(IA_{peak\ 2})_i * n(B_{ads})_{total\ i} = n(B_{ads})_{BLPE\ i} + n(B_{ads})_{BLPI\ i} + n(B_{ads})_{B3L\ i}$$
$$(IA_{peak\ 3})_i * n(B_{ads})_{total\ i} = n(B_{ads})_{BLHI\ i} + n(B_{ads})_{B5L\ i}$$

where $n(B_{ads})_{B3L}$ and $n(B_{ads})_{B5L}$ are the boron adsorbed in the form of trimer or pentamer species, respectively. With this approach we show as solid lines in Figure 11 the adjustment of the simulated values to the experimental data, shown as discrete points. In Table 6 the adjusted values for the above-defined equilibrium constants, used to simulate the data shown in Figure 11, are shown.

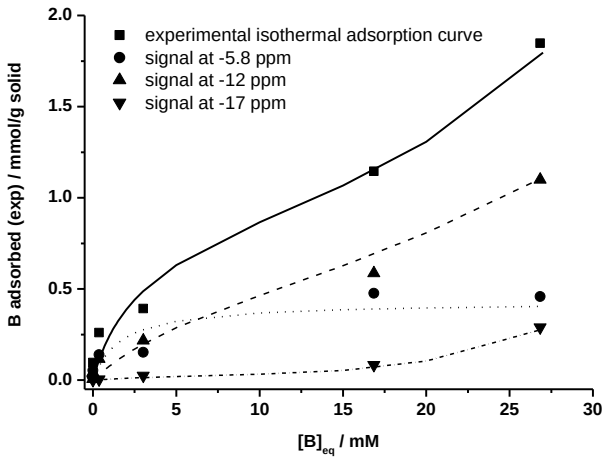

Figure 11. Isothermal boron adsorption on solid **S1**: experimental values (discrete symbols) and simulated ones (continuous lines) with the *site E*/*site I* model.

From the values in Table 6 we can see that very different adsorption constants were needed to adjust the experimental data. As previously discussed, the most stable complex formed during the boron adsorption process corresponded to the (α,β)bis-chelated species, where the monochelated ones were less stable, and the (α,γ)mono-chelated complexes were the least stable among them. Another relevant result was the poor ability of (α,β)mono-chelated complexes to displace bis-chelated ones. In relation to the coordination of oligomeric species to solid **S1**, the ability of trimer species to be adsorbed onto the attached glucose molecules was considerable and better than the ability of pentameric oligomers.

Table 6. The results obtained from the *site E*/*site I* model essayed for boron adsorption on **S1**.

log K_2 (BL2)	-0.52
log K_4 (BLPE)	-4.00
log K_5 (BLPI)	-1.00
log K_6 (BLHI)	-2.15
log K_{O3} (B3L)	-2.96
log K_{O5} (B5L)	-6.15

4. CONCLUSIONS

In short, we prepared an adsorbent for boron extraction from water by the functionalisation of a UVM7 mesoporous silica matrix with gluconamide moieties. The high affinity of boron towards polyols molecules makes this material an excellent boron adsorbent. In order to better understand the adsorption process, several solids with increasing boron contents were prepared. The ^{11}B and ^{13}C MAS NMR techniques were used to elucidate the different coordination environments when boron was adsorbed onto the **S1** material and at least three different complexes were identified: the $(\alpha,\beta)_2$-BL_2 bis-chelated complex, the (α,β)-BL monochelated complex and the (α,γ)-BL monochelated complex. Isothermal boron adsorption curves were adjusted to a model that included two different adsorption positions (*site E* and *site I*). Additional adsorption of boron oligomeric species was introduced into the model to take into account the increase in the adsorption curve in the presence of high boron concentrations. Thus by using three different coordination environments, two possible adsorption sites and with the presence of oligomeric boron species, it was possible to reproduce not only the isothermal boron adsorption curve, but also the evolution of the integrated areas for the signals in ^{11}B MAS NMR spectra obtained for the different boron containing-**S1** materials.

ACKNOWLEDGMENT

Financial support from the Spanish Government (Project MAT2009-14564-C04-01 and MAT2012-38429-C04-01) and the Generalitat Valenciana (Project PROMETEO/2009/016) is gratefully acknowledged. C.S. thanks the MICINN for a predoctoral fellowship.

REFERENCES

[1] P. D. A. Howe, *Biol. Trace Elem. Res.* 66 (1998) 153-166.

[2] WHO, Guidelines for drinking-water quality (ISBN 978 92 4 154815 1), 4th ed., Malta, (2011).

[3] J. Wolska, M. Bryjak, *Desalination* 310 (2013) 18-24.

[4] B. Wang, X. Guo, P. Bai, *Colloids Surf. A* 444 (2014) 338-344.

[5] Y. Xu, J. Q. Jiang, *Ind. Eng. Chem. Res.* 47 (2008) 16-24.

[6] T. Ben Amor, I. Dhaouadi, B. Lebeau, M. Tlili, M. Ben Amor, *Desalination* 351 (2014) 82-87.

[7] D. I. Fried, A. Schlossbauer, T. Bein, *Micropor. Mesopor. Mater*. 147 (2012) 5-9.

[8] L. Wang, T. Qi, Y. Zhang, *Colloids Surf. A*. 275 (2006) 73-79.

[9] O. Kaftan, M. Acikel, A. E. Eroglu, T. Shahwan, L. Artok, C. Ni, *Anal. Chim. Acta* 547 (2005) 31-41.

[10] J. Böeseken, *Adv. Carbohydr. Chem.* 4 (1949) 189-210.

[11] J. G. Dawber, S. I. E. Green, J. C. Dawber, S. Gabrail, *J. Chem. Soc., Faraday Trans. I* 84 (1988) 41-56.

[12] Y. Miyazaki, K. Yoshimura, Y. Miura, H. Sakashita, K. Ishimaru, *Polyhedron* 22 (2003) 909-916.

[13] K. Benner, P. Klüfers, *Carbohydr. Res.* 327 (2000) 287-292.

[14] J. G. Dawber, *J. Chem. Soc., Faraday Trans. I* 83 (1987) 771-777.

[15] M. A. Beckett, C. C. Bland, K. S. Varma, *Polyhedron* 27 (2008) 2226-2230.

[16] N. Geffen, R. Semiat, M. S. Eisen, Y. Balazs, I. Katz, C. G. Dosoretz, *J. Memb. Sci.* 286 (2006) 45-51.

[17] Y. Miyazaki, H. Matsuo, T. Fujimori, H. Takemura, S. Matsuoka, T. Okobira, K. Uezu, K. Yoshimura, *Polyhedron* 27 (2008) 2785-2790.

[18] J. G. Dawber, S. I. E. Green, *J. Chem. Soc., Faraday Trans. I* 82 (1986) 3407-3413.

[19] K. Yoshimura, Y. Miyazaki, F. Ota, S. Matsuoka, H. Sakashita, *J. Chem. Soc., Faraday Trans.* 94 (1998) 683-689.

[20] G. Rodríguez-López, M. D. Marcos, R. Martínez- Máñez, F. Sancenón, J. Soto, L. A. Villaescusa, D. Beltrán, P. Amorós, *Chem. Commun.* (2004) 2198-2199.

[21] C. Sanfeliu, R. Martínez-Máñez, F. Sancenón, J. Soto, V. Puchol, P. Amorós, M. D. Marcos, *J. Mat. Chem.* 22 (2012) 25362-25372.

[22] C. Sanfeliu, R. Martínez-Máñez, F. Sancenón, J. Soto, P. Amorós, M. D. Marcos, *Desalination* 374 (2015) 10-19.

[23] S. Cabrera, J. El Haskouri, C. Guillem, J. Latorre, A. Betrán, D. Beltrán, M. D. Marcos, P. Amorós, *Solid State Sci.* 2 (2000) 405-420.

[24] M. van Duin, J. A. Peters, A. P. G. Kieboom, H. van Bekkum, *Tetrahedron* 40 (1984) 2901-2911.

[25] M. van Duin, J. A. Peters, A. P. G. Kieboom, H. van Bekkum, *Tetrahedron* 41 (1985) 3411-3421.

[26] W. G. Henderson, M. J. How, G. R. Kennedy, E. F. Mooney, *Carbohydr. Res.* 28 (1973) 1-12.

[27] R. van den Berg, J. A. Peters, H. van Bekkum, *Carbohydr. Res.* 253 (1994) 1-12.

[28] D. G. Cory, W. M. Ritchey, *J. Magn. Reson*. 80 (1988) 128-132.

[29] L. Chu, M. I. Tejedor-Tejedor, M. A. Anderson, *Micropor. Mater.* 8 (1997) 207-213.

[30] I. C. Tilgner, P. Fischer, F. M. Bohnen, M. Rehage, W. F. Maier, *Micropor. Mater*. 5 (1995) 77-90.

[31] R. K. Iler, R. K. The Chemistry of Silica, *John Wiley & Sons, New York*, (1979).

[32] S. Brunauer, P. H. Emmet, E. Teller, *J. Am. Chem. Soc.* 60 (1938) 309-319.

[33] E. P. Barret, L. G. Joyner, P. P. Halenda, *J. Am. Chem. Soc.* 73 (1951) 373-380.

[34] M. van Duin, J. A. Peters, A. P. G. Kieboom, H. van Bekkum, *Recl. Trav. Chim. Pays-Bas* 108 (1989) 57-60.

[35] D. L. Harp, *Anal. Chim. Acta* 346 (1997) 373-379.

[36] HyperChem (TM) Professional 7.51, Hypercube, Inc., 1115 NW 4th Street, Gainesville, Florida 32601, USA.

[37] C. F. Baes, R. E. Messmer, *The hydrolysis of Cations.* Ed. John Wiley & Sons Inc, (1976).

[38] C. S. Salentine, *Inorg. Chem.* 22 (1983) 3920-3924.

[39] Solver Program, Frontline Systems, Inc (1990-2009); Optimal Methods, Inc. (1989).

[40] E. B. Simsek, B. F. Senkal, U. Beker, *Boron separation processes*, Chap 17. Ed. Elsevier, (2015).